Wavelength-Tunable Multispectral Photodetector With Both Ultraviolet and Near-Infrared Narrowband Detection Capability

Li Wang, Bo-Han Chen, Chang-Yue Fang, Jun He, Chun-Yan Wu, Xiang Zhang, Xiao-Ping Yang, Jian-Bo Mao, Ji-Gang Hu, *Member, IEEE*, and Lin-Bao Luo, *Senior Member, IEEE*

***Abstract*— The development of high-performance multispectral photodetector with narrowband and tunable spectral sensitivity is of importance but remains highly challenging to date. Here, we have reported on the fabrication of a Si Au/n-type Si/Au photodetector with tunable narrowband sensitivity not only in ultraviolet but also in near-infrared region, which is related to the controlled charge collection narrowing (CCN) mechanism. What is more, the negative response peak of the device can be readily tuned from 365 to 605 nm, and the positive response peak can be modulated from 938 to 970 nm when the bias varies from 0.1 to −0.1 V. In particular, the full-width at half-maximum is as small as 92 and 117 nm when the negative and positive response peaks approach the ultraviolet short wavelength end and near-infrared long wavelength end, respectively. The opposite polarity of the device responses in ultraviolet-visible and near-infrared regions renders the present Si photodetector potentially important in future multiple band optoelectronic systems.**

***Index Terms*— Multispectral, narrowband detection, Schottky junction, Si photodetector, wavelength tunable.**

I. Introduction

MULTISPECTRAL photodetection is very appealing for various applications, such as visual monitoring [1], criminal investigation [2], photocommunication [3], and photoplethysmography [4], due to its capability of discrimination and recognition for targets. While various studies have shown that multispectral photodetectors can be easily achieved by using some heavy and complex optical components, which will inevitably lead to relatively cumbersome detection systems, some groups have also reported that multispectral photodetectors can be fabricated by integrating devices with multi-wavelength sensitivity in a single pixel [5], [6]. For instance, wavelength-tunable multispectral photodetectors have been achieved by stacking various semiconductor materials with different bandgaps on an individual substrate [7]. These devices, however, often suffer from unfavorable lattice mismatch between different semiconductors and relatively high fabrication cost due to the use of very sophisticated epitaxy instruments [8].

Unlike the broadband photodetectors, most of the multispectral detectors are characterized by a narrowband sensitivity with a small full-width at half-maximum (FWHM) [9], which can be realized by various approaches. To name a few, reliable filterless narrowband detection has been achieved by a charge injection narrowing mechanism [10]–[12] or using photoactive materials with narrowband absorption [13]–[15]. In addition, tailoring the specific absorption of organic photoactive layers through charge collection narrowing (CCN) effect or patterning metallic nanoantennas onto semiconductor substrate has proved to be effective to achieve narrowband detection as well [19]–[22]. Despite these achievements, the majority of the spectral responsivity of narrowband photodetectors mentioned above can hardly be tuned by bias voltage [23], even though it is feasible to tune the spectral responsivity by directly adjusting the chemical compositions or architectures of the photoactive layers [24]–[26].

Here, we have demonstrated a wavelength-tunable multispectral Si photodetector with narrowband sensitivity that is related to a junction-controlled CCN mechanism (JCCN). The spectral response of the as-proposed device is controlled by not only the absorption property of the photoactive layer but also the junction structures [27], [28], which is different from that of the CCN effect related devices. It is found that the as-fabricated photodetector with simple Au/Si/Au metal–semiconductor–metal (MSM) structure possesses voltage-tunable response peak, which shows narrowband response peaks in both ultraviolet and near-infrared regions. Notably, when the bias decreases from 0.1 to −0.1 V, the negative response peak of the device can be tuned from 365 to 605 nm; meanwhile, the corresponding positive response peak can be tailored from 938 to 970 nm. This new concept device

Manuscript received February 10, 2022; revised April 13, 2022; accepted April 22, 2022. Date of publication May 6, 2022; date of current version May 24, 2022. This work was supported in part by the National Natural Science Foundation of China under Grant 62074048, Grant 62075053, Grant 92050202, and Grant U20A20216, in part by the Natural Science Foundation of Anhui Province under Grant 2108085MF229, in part by the Fundamental Research Funds for the Central Universities under Grant JZ2018-HGXC0001, in part by the Funds for the Central Universities under Grant JZ2018HGPB0275 and Grant PA2020GDKC0024, and in part by the Open Foundation of Anhui Provincial Key Laboratory of Advanced Functional Materials and Devices under Grant 4500-411104/011. The review of this article was arranged by Editor S.-C. Shen. *(Corresponding authors: Li Wang; Lin-Bao Luo.)*

Li Wang, Bo-Han Chen, Chang-Yue Fang, Jun He, Chun-Yan Wu, Xiang Zhang, Xiao-Ping Yang, Jian-Bo Mao, and Lin-Bao Luo are with the School of Microelectronics, Hefei University of Technology, Hefei 230009, China (e-mail: wlhgd@hfut.edu.cn; luolb@hfut.edu.cn).

Ji-Gang Hu is with the School of Physics, Hefei University of Technology, Hefei, Anhui 230009, China.

Color versions of one or more figures in this article are available at https://doi.org/10.1109/TED.2022.3171501.

Digital Object Identifier 10.1109/TED.2022.3171501

0018-9383 © 2022 IEEE. Personal use is permitted, but republication/redistribution requires IEEE permission.
See https://www.ieee.org/publications/rights/index.html for more information.

Authorized licensed use limited to: HEFEI UNIVERSITY OF TECHNOLOGY. Downloaded on September 18,2022 at 08:59:11 UTC from IEEE Xplore. Restrictions apply.

will open up new opportunities of the development of other narrowband photodetectors for future optoelectronic system applications.

II. Experimental Details

The multispectral photodetector was fabricated on commercially available double-side polished n-type (100) Si wafer. After the natural oxide layer of the wafer was removed by immersing the wafer into buffered oxide etchant solution ($HF:NH_4F:H_2O = 3$ mL:6 g:10 mL) for 5 min, two Au electrodes (1×1 mm^2, thickness of 50 nm) were deposited on both sides of wafer in a high-vacuum electron-beam evaporation system [as shown in Fig. 1(a)]. Then, an illumination area of 1 mm $\times$ 150 μm was defined on the upper surface of wafer with opaque tape for subsequent photoelectric property measurement.

Electrical measurements of the device were carried on a semiconductor characterization system (Keithley 2400). Also, laser diodes of different wavelengths (Thorlabs, M365L3, M530L3, and M970L3) were used as light sources. Spectral response was measured with a lab-built optoelectronic system consisted of a light source (LE-SP-LS-XE) and monochromator (LE-SP-M300). The intensity of light sources was carefully calibrated using a power meter (Thorlabs GmbH., PM 100D) before measurement. In addition, a laser diode driver (Thorlabs, DC2200) and an oscilloscope (Tektronix, TDS2012B) were employed to study the response speed of the device. All measurements were performed under ambient conditions at room temperature.

The corresponding simulation of the photogeneration rate and photon absorption rate in Si substrate was carried out using Silvaco TCAD. The 2-D structure of n-type phosphorous-doped (100) Si substrate (5×10^{14} cm^{-3}) with the dimension of 10×200 μm^2 was constructed. Also, grid points number of $\sim$10 000 was chosen to balance the time and accuracy of computation. The Shockley–Read–Hall model and the optical model were adopted for the generation–recombination processes modeling. A beam of light was introduced to the upper surface of Si wafer at an incident angle of 90°.

III. Results and Discussion

As shown in the schematic of device [see Fig. 1(a)], the two identical Au/n-Si Schottky junctions on the upper and lower surfaces of the n-type silicon wafer are labeled as junctions 1 and 2, respectively. TCAD simulation results show that the photogeneration rate under shorter wavelength light decays rapidly as light goes deep into silicon, whereas longer wavelength light can produce photogenerated carriers more evenly [inset in Fig. 1(a)]. Therefore, junction 1 on light incident surface should prefer to show response to shorter wavelength light according to the JCCN mechanism, while junction 2 will be more sensitive to the longer wavelength light, which can reach its depletion region. This is supported by the plots of photon absorption rate versus wavelength at different depths in silicon substrate [see Fig. 1(b)]. The absorption peak moves from short wavelength to long one with the increase of depth. Such a depth-dependent absorption peak is reasonable considering the fact that the absorption

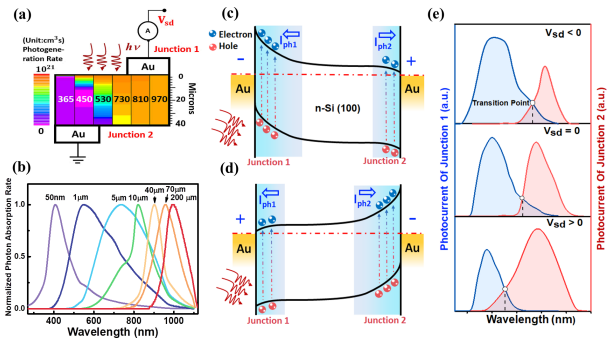

Fig. 1. (a) Schematic of the photodetector based on Si MSM structure; Inset: photogeneration rate as a function of incident light wavelength and depth in Si. (b) Simulated normalized photon absorption rate versus wavelength at different depths in Si. Energy band diagrams of the device under light illumination at (c) negative bias ($V_{sd} < 0$) and (d) positive bias ($V_{sd} > 0$). (e) Schematic photocurrent of two back-to-back Schottky junctions versus wavelength under $V_{sd} < 0$, $V_{sd} = 0$, and $V_{sd} > 0$.

coefficient of a semiconductor material is mainly determined by wavelength of incident light, and the absorption coefficient of Si corresponding to UV light is at least 2–3 orders of magnitude larger than that for visible light, according to the Beer–Lambert law [19]. This sharp distinction in absorption coefficient for different wavelengths can lead to UV absorption at very superficial surface of Si wafer, but visible light absorption at very deep area of the Si [29].

Actually, the photocurrent directions of junctions 1 and 2, which jointly determine the spectral response of the device, are opposite to each other [30] [as shown in Fig. 1(c) and (d)]. For convenience, the direction of junction 2 photocurrent (I_{ph2}) is set to be positive. When the values of the two junctions current are equal, there will be a transition point appeared, where the polarity of total device current begins to change. Fig. 1(c) shows that negative bias can enhance the built-in electric field of junction 1 and widen its depletion region [31], with the depletion region of junction 2 narrowing at the same time and vice versa [see Fig. 1(d)]. As shown in Fig. 1(b), the wider the depletion region of Schottky junction, the broader its spectral response range. When bias changes from negative to positive, photoresponse of junction 2 will gradually dominate over a wider wavelength range [see Fig. 1(e)]. Thus, when the transition point moves from long to short wavelength, it is possible to achieve narrowband detection of long wavelength under negative bias, because of the reduction in spectral response range of junction 2 and the broadening of junction 1 spectral response range. Similarly, narrowband detection of short wavelength light can be obtained under positive bias.

The relation between the wavelength and bias voltage of transition point is confirmed by the I–V curves of the device based on 40 μm substrate under illumination of different wavelength lights [see Fig. 2(a)–(c)]. Unlike 0 V in dark field, the bias voltage of the transition point, where the device current changes from negative to positive, decreases monotonously from 0.12 to -0.06 V, as the wavelength of incident light increases from 365 to 970 nm. Moreover, the voltage of transition point keeps almost unchanged when the light wavelength is fixed and the light intensity varies in a relatively large range (10^{-6}–10^{-1} W/cm^2). This is important to the practical application of the device based on the JCCN mechanism.

Authorized licensed use limited to: HEFEI UNIVERSITY OF TECHNOLOGY. Downloaded on September 18,2022 at 08:59:11 UTC from IEEE Xplore. Restrictions apply.

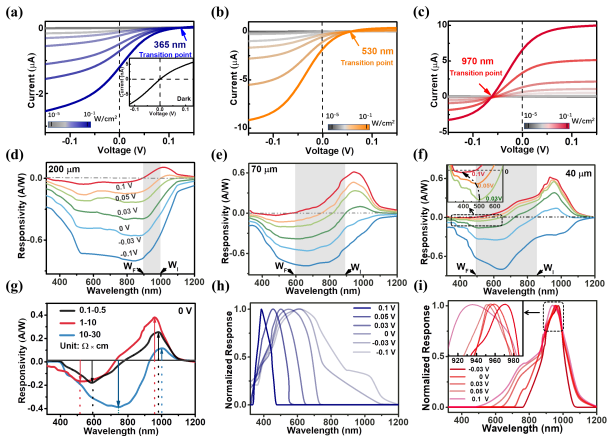

Fig. 2. I–V curves of the device (40 μm, 1–10 $\Omega \cdot$ cm) under (a) 365, (b) 530, and (c) 970 nm illumination with different intensities. Inset: corresponding I–V curve in the dark. Spectral responsivities of the devices with Si substrate of (d) 200, (e) 70, and (f) 40 μm under bias from −0.1 to 0.1 V. (g) Wavelength-dependent responsivities of the 40 μm devices with substrates of different resistivity at zero bias. Normalized (h) negative and (i) positive responsivity absolute values of the device (40 μm, 1–10 $\Omega \cdot$ cm) versus wavelength under different biases.

To further shed light on the effect of silicon substrate thickness on spectral response, the device with thickness of 200, 70, and 40 μm was tested [see Fig. 2(d)–(f)]. It is shown that, as bias voltage increases from −0.1 to 0.1 V, the gap between the wavelengths of initial transition point (W_I) and the final transition point (W_F) becomes wider with the decrease of silicon substrate thickness. The transition point can be adjusted over a larger wavelength range in device of thinner substrate, which should be caused by the bigger spectral response overlap of the two Schottky junctions in the thinner substrate. Thus, different from the broad spectrum of 200 μm device under most bias voltage, the device of 40 μm exhibits obvious negative and positive peak responses [see Fig. 2(f)]. Furthermore, the wavelength of the positive response peak at long wavelength end increases with the thickness of Si substrate under bias voltage of 0.1 V [see Fig. 2(d)–(f)]. This agrees well with the simulation results of Fig. 1(b). Similar phenomenon has been observed in narrowband photodetector of single Schottky junction too [28].

In addition, both negative and positive response peaks show blue shift as the bias changes from negative to positive [see Fig. 2(f)]. Similar blue-shift phenomenon can be observed as well when the doping concentration of silicon substrate increases [see Fig. 2(g)]. These should be the results of the relatively improved photoelectric conversion capability of junction 2 compared with junction 1 [32]. Fig. 2(h) and (i) shows the negative and positive responsivity absolute values of the device (40 μm, 1–10 $\Omega \cdot$ cm) versus wavelength under different biases. It can be seen that the negative response peak shifts from 605 to 365 nm with FWHM decreasing from 400 to 92 nm, as the bias voltage increases from −0.1 to 0.1 V [see Fig. 2(h)]. Meanwhile, the positive response peak moves from 938 to 970 nm with the shrink of FWHM from 206 to 119 nm when the bias voltage decreases from 0.1 to −0.03 V [see Fig. 2(i)]. It should be noted that the narrowband detection of 365 and 970 nm light can be readily switched to by changing the bias voltage.

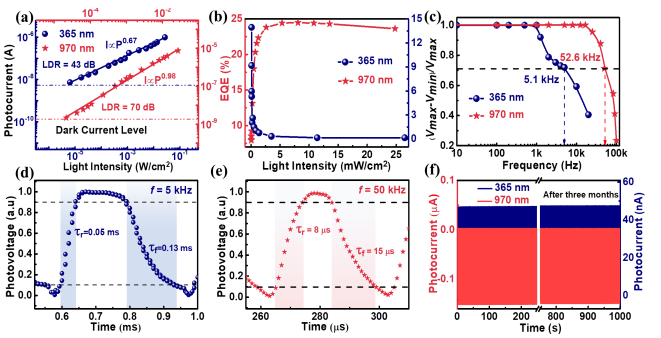

Fig. 3. Narrowband detection performance of the device under the illumination of 365 and 970 nm at 0.1 and −0.03 V, respectively. (a) Linear dynamic range of the device. (b) EQE as a function of light intensity. (c) Relative balance $(V_{max} - V_{min})/V_{max}$ as a function of light modulation frequency. Corresponding single magnified photoresponse for determining the rise/fall times at (d) 5 (365 nm) and (e) 50 kHz (970 nm). (f) Time-dependent photoresponse for about 500 cycles of operation and after three months storage under ambient condition (365 nm, 0.1 V, 7.53 mW/cm^2; 970 nm, −0.03 V, 0.69 mW/cm^2).

Under the corresponding bias of −0.03 and 0.1 V, the narrowband detection performance of the device at 970 and 365 nm was further tested, respectively. Limited by the maximum intensity of light sources, the linear dynamic ranges of the device are evaluated to be 70 (970 nm) and 43 dB (365 nm). A general power law, $I_{ph} = P^{\theta}$, was used to fit the dependence of photocurrent on light intensity, where θ is the empirical value reflecting the recombination of the photoexcited carriers, I_{ph} denotes the net photocurrent ($I_{ph} = I_{light} - I_{dark}$), and P denotes the light intensity [33]. The smaller θ value (0.67) of 365 nm than 970 nm (0.98) indicates that the detection of 365 nm is more affected by surface recombination, which should be due to the ultrathin distribution region of its photogenerated carriers close to light incident surface.

When light intensity decreases, the external quantum efficiency (EQE) of the device increases to 13.6% under the illumination of 365 nm [see Fig. 3(b)]. Under 970 nm illumination, the EQE value, however, drops sharply from 24.5% when the light intensity is lower than 2.2 mW/cm^2. Based on the rationale outlined above, the response of 970 nm light is substantially dominated by junction 2 [see Fig. 1(b)]; its abnormal decrease of EQE is understandable considering the sharply increased proportion of photocurrent generated by junction 1 in the total device current under low light intensity. Furthermore, high-frequency performance test shows that the 3 dB frequency of the device under 365 and 970 nm illumination is 5.1 and 52.6 kHz with response time comparable to that of the broadband photodetector at corresponding spectral range [see Fig. 3(c)–(e)] [34]–[36]. The narrowband detection of 365 and 970 nm light exhibits high stability, which can keep good repeatability even after three months [see Fig. 3(f)].

IV. Conclusion

In summary, we have presented a multispectral wavelength-tunable Si photodetector of simple MSM structure, which shows obvious peak response in both ultraviolet-visible and near-infrared regions. The wavelength and FWHM of its response peak can be tuned effectively in large range under low bias, especially at short and long wavelength ends. The long wavelength end of the device spectral response is

Authorized licensed use limited to: HEFEI UNIVERSITY OF TECHNOLOGY. Downloaded on September 18,2022 at 08:59:11 UTC from IEEE Xplore. Restrictions apply.

determined by Si substrate and bias voltage. Its narrowband detection at 365 and 970 nm exhibits good linearity, high stability, and repeatability. Considering the high compatibility with Si microelectronic technology and simple architecture of the device, it should be practical and competitive in multispectral photodetection.

REFERENCES

[1] M. Dong, B. Wang, M. Ren, C. Zhang, W. Zhao, and R. Albarracin, "Joint visualization diagnosis of outdoor insulation status with optical and acoustical detections," *IEEE Trans. Power Del.*, vol. 34, no. 4, pp. 1221–1229, Aug. 2019, doi: 10.1109/TPWRD.2018.2870080.

[2] X. Tang, M. M. Ackerman, M. Chen, and P. Guyot-Sionnest, "Dual-band infrared imaging using stacked colloidal quantum dot photodiodes," *Nature Photon.*, vol. 13, no. 4, pp. 277–282, Apr. 2019, doi: 10.1038/s41566-019-0362-1.

[3] M. M. Fan, K. L. Xu, X. Y. Li, G. H. He, and L. Cao, "Self-powered solar-blind UV/visible dual-band photodetection based on a solid-state PEDOT: PSS/a-Ga_2O_3 nanorod array/FTO photodetector," *J. Mater. Chem. C*, vol. 9, no. 46, pp. 16459–16467, Dec. 2021, doi: 10.1039/d1tc04091j.

[4] S. Ramona Vulcan, S. André, and M. Bruyneel, "Photoplethysmography in normal and pathological sleep," *Sensors*, vol. 21, p. 2928, Apr. 2021, doi: 10.3390/s21092928.

[5] A. M. Hoang, A. Dehzangi, S. Adhikary, and M. Razeghi, "High performance bias-selectable three-color short-wave/mid-wave/long-wave infrared photodetectors based on type-II InAs/GaSb/AlSb superlattices," *Sci. Rep.*, vol. 6, no. 1, Apr. 2016, Art. no. 024144, doi: 10.1038/srep24144.

[6] H. S. Ling, S. Y. Wang, W. C. Hsu, and C. P. Lee, "Voltage-tunable dual-band quantum dot infrared photodetectors for temperature sensing," *Opt. Exp.*, vol. 20, no. 10, pp. 10484–10489, May 2012, doi: 10.1364/OE.20.010484.

[7] J. N. Deng *et al.*, "Integration of MoS_2 with InAlAs/InGaAs heterojunction for dual color detection in both visible and near-infrared bands," *Adv. Opt. Mater.*, vol. 7, no. 23, Dec. 2019, Art. no. 1901039, doi: 10.1002/adom.201901039.

[8] M. Dai *et al.*, "A dual-band multilayer InSe self-powered photodetector with high performance induced by surface plasmon resonance and asymmetric Schottky junction," *ACS Nano*, vol. 12, no. 8, pp. 8739–8747, Aug. 2018, doi: 10.1021/acsnano.8b04931.

[9] S. Xing *et al.*, "Miniaturized VIS-NIR spectrometers based on narrowband and tunable transmission cavity organic photodetectors with ultrahigh specific detectivity above 10^{14} Jones," *Adv. Mater.*, vol. 33, no. 44, Nov. 2021, Art. no. 2102967, doi: 10.1002/adma.202102967.

[10] Z. J. Zhao *et al.*, "Highly sensitive narrowband photomultiplication-type organic photodetectors prepared by transfer-printed technology," *Adv. Funct. Mater.*, vol. 31, no. 43, Oct. 2021, Art. no. 2106009, doi: 10.1002/adfm.202106009.

[11] M. Liu *et al.*, "Highly sensitive, broad-band organic photomultiplication-type photodetectors covering UV-Vis-NIR," *J. Mater. Chem. C*, vol. 9, no. 19, pp. 6357–6364, 2021, doi: 10.1039/d1tc00555c.

[12] K. X. Yang *et al.*, "Highly sensitive photomultiplication type polymer photodetectors by manipulating interfacial trapped electron density," *Chem. Eng. J.*, vol. 435, no. 2, May 2022, Art. no. 134973, doi: 10.1016/j.cej.2022.134973.

[13] Q. Xiong, F. I. Chowdhury, and X. Wang, "Filter-free narrowband photodetectors employing colloidal quantum dots," *IEEE J. Sel. Topics Quantum Electron.*, vol. 24, no. 2, pp. 1–6, Mar. 2018, doi: 10.1109/JSTQE.2017.2776522.

[14] L. Gao *et al.*, "Flexible filter-free narrowband photodetector with high gain and customized responsive spectrum," *Adv. Funct. Mater.*, vol. 27, no. 33, Sep. 2017, Art. no. 1702360, doi: 10.1002/adfm.201702360.

[15] S. Yoon, Y.-H. Ha, S.-K. Kwon, Y.-H. Kim, and D. S. Chung, "Fabrication of high performance, narrowband blue-selective polymer photodiodes with dialkoxynaphthalene-based conjugated polymer," *ACS Photon.*, vol. 5, no. 2, pp. 636–641, Feb. 2018, doi: 10.1021/acsphotonics.7b01248.

[16] X. Nie *et al.*, "Strongly polarized quantum well infrared photodetector with metallic cavity for narrowband wavelength selective detection," *Appl. Phys. Lett.*, vol. 116, no. 16, Apr. 2020, Art. no. 161107, doi: 10.1063/5.0002012.

[17] M.-R. Tang, H.-H. Hsiao, C.-H. Hong, W.-L. Huang, and S.-C. Lee, "An uncooled LWIR-detector with LSPR enhancement and selective narrow absorption," *IEEE Photon. Technol. Lett.*, vol. 30, no. 13, pp. 1206–1209, Jul. 1, 2018, doi: 10.1109/LPT.2018.2839650.

[18] A. Sobhani *et al.*, "Narrowband photodetection in the near-infrared with a plasmon-induced hot electron device," *Nature Commun.*, vol. 4, no. 1, p. 1643, Mar. 2013, doi: 10.1038/ncomms2642.

[19] J. Wang *et al.*, "Self-driven perovskite narrowband photodetectors with tunable spectral responses," *Adv. Mater.*, vol. 33, no. 3, Jan. 2021, Art. no. 2005557, doi: 10.1002/adma.202005557.

[20] J. Li *et al.*, "Self-trapped state enabled filterless narrowband photodetections in 2D layered perovskite single crystals," *Nature Commun.*, vol. 10, no. 1, pp. 1–10, Feb. 2019, doi: 10.1038/s41467-019-08768-z.

[21] M. R. Esopi, E. Zheng, X. Zhang, C. Cai, and Q. Yu, "Tuning the spectral response of ultraviolet organic–inorganic hybrid photodetectors via charge trapping and charge collection narrowing," *Phys. Chem. Chem. Phys.*, vol. 20, no. 16, pp. 11273–11284, Apr. 2018, doi: 10.1039/c8cp00361k.

[22] D. Periyanagounder *et al.*, "Fast-response, highly air-stable, and water-resistant organic photodetectors based on a single-crystal Pt complex," *Adv. Mater.*, vol. 32, no. 2, Jan. 2020, Art. no. e1904634, doi: 10.1002/adma.201904634.

[23] J. Miao, F. Zhang, M. Du, W. Wang, and Y. Fang, "Photomultiplication type organic photodetectors with broadband and narrowband response ability," *Adv. Opt. Mater.*, vol. 6, no. 8, Apr. 2018, Art. no. 1800001, doi: 10.1002/adom.201800001.

[24] Y. Fang, Q. Dong, Y. Shao, Y. Yuan, and J. Huang, "Highly narrowband perovskite single-crystal photodetectors enabled by surface-charge recombination," *Nature Photon.*, vol. 9, pp. 679–686, Aug. 2015, doi: 10.1038/nphoton.2015.156.

[25] M. Tanzid *et al.*, "Combining plasmonic hot carrier generation with free carrier absorption for high-performance near-infrared silicon-based photodetection," *ACS Photon.*, vol. 5, no. 9, pp. 3472–3477, Sep. 2018, doi: 10.1021/acsphotonics.8b00623.

[26] A. Solanki, S. Li, H. Park, and K. B. Crozier, "Harnessing the interplay between photonic resonances and carrier extraction for narrowband germanium nanowire photodetectors spanning the visible to infrared," *ACS Photon.*, vol. 5, no. 2, pp. 520–527, Feb. 2018, doi: 10.1021/acsphotonics.7b01034.

[27] L. Wang *et al.*, "Self-powered filterless narrow-band p–n heterojunction photodetector for low background limited near-infrared image sensor application," *ACS Appl. Mater. Interfaces*, vol. 12, no. 19, pp. 21845–21853, May 2020, doi: 10.1021/acsami.0c02827.

[28] L. Wang *et al.*, "Highly sensitive narrowband Si photodetector with peak response at around 1060 nm," *IEEE Trans. Electron Devices*, vol. 67, no. 8, pp. 3211–3214, Aug. 2020, doi: 10.1109/TED.2020.3001245.

[29] E. K. Liu, B. S. Zhu, and J. S. Liu, *The Physics of Semiconductors*. Beijing: PHEI, Apr. 2011, p. 260.

[30] A. De Iacovo, A. Ballabio, J. Frigerio, L. Colace, and G. Isella, "Design and simulation of Ge-on-Si photodetectors with electrically tunable spectral response," *J. Lightw. Technol.*, vol. 37, no. 14, pp. 3517–3525, Jul. 15, 2019, doi: 10.1109/JLT.2019.2917590.

[31] E. K. Liu, B. S. Zhu, and J. S. Liu, *The Physics of Semiconductors*. Beijing, China: PHEI, Apr. 2011, p. 223.

[32] G. Masini, L. Colace, F. Galluzzi, G. Assanto, T. P. Pearsall, and H. Presting, "Voltage tunable SiGe photodetector: A novel tool for crypted optical communications through wavelength mixing," *Appl. Phys. Lett.*, vol. 70, no. 24, pp. 3194–3196, Jun. 1997, doi: 10.1063/1.119155.

[33] C. Y. Wu *et al.*, "Defect-induced broadband photodetection of layered γ-In_2Se_3 nanofilm and its application in near infrared image sensors," *J. Mater. Chem. C*, vol. 7, no. 37, pp. 11532–11539, Oct. 2019, doi: 10.1039/c9tc04322e.

[34] Y. Zhang, J. Chen, L. Zhu, and Z. L. Wang, "Self-powered high-responsivity photodetectors enhanced by the pyro-phototronic effect based on a $BaTiO_3$/GaN heterojunction," *Nano Lett.*, vol. 21, no. 20, pp. 8808–8816, Oct. 2021, doi: 10.1021/acs.nanolett.1c03171.

[35] J.-H. Kim *et al.*, "Solution-processed near-infrared Cu(in,Ga)$(S,Se)_2$ photodetectors with enhanced chalcopyrite crystallization and bandgap grading structure via potassium incorporation," *Sci. Rep.*, vol. 11, no. 1, pp. 1–10, Apr. 2021, doi: 10.1038/s41598-021-87359-9.

[36] J. H. Guo *et al.*, "Few-layer organic crystalline van der Waals heterojunctions for ultrafast UV phototransistors," *Adv. Electron. Mater.*, vol. 6, no. 6, Jun. 2020, Art. no. 2000062, doi: 10.1002/aelm.202000062.

Authorized licensed use limited to: HEFEI UNIVERSITY OF TECHNOLOGY. Downloaded on September 18,2022 at 08:59:11 UTC from IEEE Xplore. Restrictions apply.